Supplementary Methods for "Mineral dust aerosol impacts on global climate and climate change"

Jasper F. Kok[1,*], Trude Storelvmo[2], Vlassis A. Karydis[3], Adeyemi A. Adebiyi[4], Natalie M. Mahowald[5], Amato T. Evan[6], Cenlin He[7], and Danny M. Leung[1]

[1]Department of Atmospheric and Oceanic Sciences, University of California, Los Angeles, CA 90095, USA
[2]Department of Geoscience, University of Oslo, 0315 Oslo, Norway
[3]Inst. for Energy and Climate Research, IEK-8, Forschungszentrum Jülich, Jülich 52425, Germany
[4]Department of Life and Environmental Sciences, University of California, Merced, CA, 95344, USA.
[5]Department of Earth and Atmospheric Sciences, Cornell University, Ithaca, NY, 14850, USA.
[6]Scripps Institution of Oceanography, University of California, San Diego, CA 92093
[7]Research Applications Laboratory, National Center for Atmospheric Research, Boulder, CO 80301, USA

[*]Corresponding author: jfkok@ucla.edu

We reconstructed atmospheric dust loading between the years 1841-2000 by combining a compilation of dust deposition records with constraints on the deposition flux produced by each of nine major source regions to each deposition site. These constraints on source-resolved deposition fluxes were obtained from the Dust Constraints from joint Observational-Modelling-Experimental analysis (DustCOMM) data set. This data set includes uncertainties on deposition fluxes that comparisons against independent data suggest are realistic[1,2].

Our approach is an extension of the methodology used in Mahowald et al.[3], who also used a compilation of dust deposition records to reconstruct dust loading. We improved upon the approach in Mahowald et al.[3] in a number of ways. First, we used almost double the number of dust deposition records (19 versus 11), including several recently published records that constrain dust from North Africa and East Asia[4-9]. These two source regions together account for ~60% of global dust loading[2] but most deposition records constraining these two regions were not available in Mahowald et al.[3]. Second, we used explicit constraints on the contributions of the different source regions to the deposition flux at each site, allowing a statistical approach that finds the most likely evolution of dust loading over time for each of nine major dust source regions[1,2]. Finally, we used a bootstrap approach with resampling to propagate errors in both deposition flux records and in the DustCOMM source region-resolved deposition fluxes[10,11].

Below, we first describe the compilation of dust deposition records, after which we describe the methodology for reconstructing dust loading.

Compilation of dust deposition records

To construct our compilation of dust deposition records, we built on the compilation of 25 deposition records obtained by Hooper and Marx[12]. Each of these records span at least 150 years of the pre-industrial to modern climate, ends after 1975, and has a time resolution of at least one data point per 10 years. Some of these records are based on measurements of dust particles in a sedimentary matrix (e.g., ice) and some are based on proxies for dust, such as the concentration of crustal elements like Mg and Ca. Measurements of the concentration of dust or a dust proxy are then converted to a dust deposition flux by calculating the mass accumulation rate of the sedimentary matrix using an age model that links the depth of the sediment to its age (e.g., Ref. [13]). We use a subset of 13 of these deposition records, all of which Hooper and Marx[12] identified as being dominated by long-range transported dust, rather than by locally generated dust (also see discussion in Mahowald et al.[3]). Note that these 13 records exclude three dust records from Antarctic ice cores that were used in Hooper and Marx[12] but that were affected by local dust

emissions (WAIS[14] and Mount Erebus[15]) or that are unpublished data sets (Siple Dome). Because these 13 records included only one record dominated by North African dust[6], we added four more published deposition records dominated by North African dust, namely records from Barbados[4], the Swiss-Italian Alps[5], Corsica[7], and Cape Verde[16]. Additionally, we added deposition records from the northern Antarctic Peninsula[17] and the Colorado mountains[18], both of which were used by Mahowald et al.[3]. All deposition records used in this study are listed in Table S1.

Data from all deposition records were processed as follows. First, the data from each deposition record were linearly interpolated to obtain annual values in the period 1841-2000, after which all fluxes were normalized to the value of the median dust flux in the period 1991-2000. If the record was missing data, either at the start or end of the 1841-2000 period, then these data points were filled in by taking the median of the 10 years most proximal to the missing data. We then took the median dust flux for each decade to reduce the substantial noise and year-to-year variability contained in some deposition records, which might be due to various factors unrelated to changes in dust emitted from large source regions (see Refs. [2,19,20] and further discussion below).

An exception on the data processing procedure above was made for the Cape Verde record of Evan & Mukhopadhyay[16]. This data set is unusual in that its accuracy was confirmed by correlation with satellite-observed aerosol optical depth data, but this data set also only spans the period 1955 – 2000. To fill in this record in the period 1841-1954, we used the mean of the normalized fluxes for the four other records that are dominated by North African dust, namely from Mauritania Canyon[6], the Bahamas[4], the Swiss-Italian Alps[5], and Corsica[7]. We then normalized the mean of those four records such that the dust flux over the period 1955-1974 equaled that of the Evan & Mukhopadhyay[16] record.

Reconstruction of dust loading since pre-industrial times

We used the compilation of dust deposition records to reconstruct the historical changes in dust loading generated by each of nine source regions. To do so, we used the DustCOMM data constraints on the relative contribution of each source region to each deposition core site in the modern climate (Fig. S1). That is, given the compilation of deposition flux timeseries, we obtained the evolution of normalized dust loading per source region that minimizes the disagreement between the deposition flux timeseries and the reconstructed dust loading. Specifically, we obtained the time evolution of dust loading generated by each source region by finding, for each decade, the values that minimizes the cost function[1]

$$\chi(t)^2 = \sum_{j=1}^{N_{\mathrm{dep}}} \left[\sum_{i=1}^{N_{\mathrm{sr}}} \lambda_i(t) \hat{f}_{i,j}^{\mathrm{cc}} - \tilde{\beta}_j(t) \right]^2 , \tag{S1}$$

where $N_{\mathrm{dep}} = 19$ is the number of deposition flux timeseries in the compilation (Table S1) and $N_{\mathrm{sr}} = 9$ is the number of source regions, which are western North Africa, eastern North Africa, the Southern Sahara and Sahel, the Middle East & Central Asia, East Asia, North America, Australia, South America, and Southern Africa (see Fig. S1 and Ref. [1]). Together, these 9 source regions account for the vast majority of natural dust emissions[1]. However, emissions from high latitudes (~2-3% of global emissions[21]) and from anthropogenic activities like industrial processes and vehicular traffic on dirt roads are not included[22]. Furthermore, $\hat{f}_{i,j}^{\mathrm{cc}}$ is the DustCOMM constraint on source region *i*'s fractional contribution to deposition site *j* in the current climate, and $\tilde{\beta}_j(t)$ is the measured deposition flux at site *j* for decade *t,* normalized by the median dust deposition flux in the period 1991-2000. Finally, $\lambda_i(t)$ is the normalized globally integrated dust loading generated by source region *i*,

$$\lambda_i(t) = \frac{L_i(t)}{L_i^{cc}}, \tag{S2}$$

where $L_i(t)$ is the dust loading generated by source region *i* in decade *t* and L_i^{cc} is the DustCOMM constraint on the dust loading generated by source region *i* in the modern climate (see Table 1 in Ref.[2]). Because the DustCOMM constraints were obtained for the years 2004-2008, here we need to assume that

dust loading in the period 1991-2000 equals that in the period 2004-2008, which introduces additional error in our results. Furthermore, Eqs. (S1) and (S2) assume that a source region's deposition flux scales linearly with its globally integrated dust loading.

Note that the solution for Eq. (S1) is over-constrained, with 19 deposition cores and only nine source regions, which helps reduce errors on $\lambda_i(t)$. Nonetheless, because deposition fluxes from the Western North Africa, Eastern North Africa, and Sahel source regions tend to be correlated, and because of a dearth of deposition records dominated by dust from the Sahel and Eastern North Africa, we cannot separately constrain the Western North Africa (i = 1), Eastern North Africa (i = 2), and Sahel (i = 3) source regions. Therefore, we grouped these three source regions into a single source region similar to the North Africa source region used in Mahowald et al.[3], meaning that we forced $\lambda_1(t) = \lambda_2(t) = \lambda_3(t)$ when solving (S1). Furthermore, we keep the Southern Africa source region (i = 9) constant (i.e., $\lambda_9(t) = 1$) because none of the deposition records are dominated by dust from this relatively minor source region (~1-2% of global dust loading[2]), making its temporal evolution under-constrained.

Measurements of deposition fluxes and DustCOMM constraints on the relative contribution of each source region both carry substantial uncertainties[2,23-25]. We propagated these uncertainties into $\lambda_i(y)$ and thus into the reconstruction of each source region's globally integrated loading using a bootstrap procedure[10,11] in which we resample the deposition sites. Specifically, we repeat the following steps (also see Ref.[1]) a large number of times (~1,000):

1. We obtain a realization of the 3D global dust cycle, including the source region-resolved deposition flux to each deposition site, per the procedure detailed in Kok et al.[1] (see especially section 2.4 in Ref. [1]). From this realization, we obtain $\hat{f}_{i,j}^{cc}$ and L_i^{cc}.
2. We randomly draw, with replacement, 19 cores from our compilation of 19 cores. As such, for each iteration, some cores will be used not at all, some only once, and some more than once. This resampling procedure propagates uncertainty due to errors in the dust deposition records and yields $\tilde{\beta}_j(y)$.
3. We use equation S1 to obtain $\lambda_i(t)$, the globally integrated normalized dust loading for each source region. To prevent unrealistic solutions from propagating into our results, for instance for when a random drawing of deposition cores in step 2 results in one or more source regions being poorly constrained, we only use an iteration's result if the change in the dust loading due to each source region is less than a factor of five (i.e., $\min\left(\frac{L_i(t)}{L_i^{cc}}\right) > 0.2$ and $\max\left(\frac{L_i(t)}{L_i^{cc}}\right) < 5$).
4. We use equation S2 to calculate $L_i(t)$ and the time evolution of the globally integrated dust loading as $L_{\mathrm{glb}}(t) = \sum_{i=1}^{N_{\mathrm{sr}}} L_i(t)$.

This approach yields a large number of realizations that represent the probability distribution of $L_i(t)$ and $L_{\mathrm{glb}}(t)$. We report the median and one standard error range of these results in Figures 4 and 5 in the main text. Additionally, we show the resulting comparisons against each of the 19 deposition cores in Fig. S2 and the reconstructed loading for each source region in Fig. S3. We also compare the dust reconstruction against long-term dust surface concentration measurements made since the 1970s at Barbados and Miami in Fig. S4. The dust reconstruction is in excellent agreement with the Barbados record (Fig. S4a) and captures the trend in the Miami record, although it underestimates the magnitude of the peak dust loading in the 1980s there (Fig. S4b).

As discussed in more detail in Mahowald et al.[3], using deposition cores to reconstruct global dust loading requires a number of critical assumptions that could introduce large errors in the results, not all of which are quantified by our error propagation procedure. First, our methodology assumes that the spatial pattern of the dust deposition flux per source region has not changed since pre-industrial times. This is likely inaccurate, as the historical increase in dust loading suggests that new source regions have been activated over time, either by climate or human land use changes. However, the effect of this limitation on our results might be limited because variability of simulated dust emissions in even the modern climate is

very large (e.g., Figure 2 in Ref.[26]) and DustCOMM draws on simulations from six different global models. Because satellite analyses indicate that ~25% of present day emissions are generated from surfaces with substantial human land use[27] it thus appears unlikely that the difference in the spatial pattern between dust emissions in the modern and pre-industrial period will be large compared to the substantial diversity in the spatial pattern of emissions that is already accounted for by DustCOMM. Second, measurements and simulations of dust deposition fluxes are subject to large experimental and representation errors[23,26,28], which could cause further errors in the reconstruction of global dust loading. Our approach of using relative changes in dust deposition over time at each deposition site addresses this concern somewhat as errors in trends of dust deposition fluxes are usually substantially lower than in absolute values[4]. Third, trends in dust fluxes at deposition sites might not reflect trends in dust emissions but instead in dust transport pathways[19] and in the precipitation that drives wet deposition[29]. However, ice core records indicate that rates of sea-salt aerosol deposition have remained approximately constant since pre-industrial times, which indicates that wet deposition rates have not changed substantially[30]. The effect of possible changes in dust transport pathways are difficult to quantify and it is possible that a trend in deposition data at a given site is due to long-term changes in dust transport pathways rather than changes in emissions. This concern about changes in transport causing spurious trends in deposition data is ameliorated somewhat by our use of deposition data from 19 deposition sites (Table 1). That is, because the bias caused by changes in transport pathways will differ for each site it constitutes a random error, the effect of which is thus reduced with more data. Also note that this random error is inherently propagated into our results by the bootstrap procedure with resampling. Fourth, trends in deposition fluxes will not be reflective of trends in major source regions if dust from a deposition site is dominated by local dust or by dust from a non-representative subsection of a major source region[29]. Errors in the classification of which deposition records are reflective of long-range transported dust from major source regions[3,12] could thus cause errors in the dust reconstruction. Also note that more deposition records could facilitate a substantially more accurate dust reconstruction because it could allow the use of smaller source regions in solving Eq. (S1); for instance, more deposition records could allow the temporal evolution of the western North Africa, eastern North Africa, and Southern Sahara and Sahel to be solved without combining these source regions. Considering these potentially substantial sources of uncertainty, the error estimates on our reconstructed global dust loading should be considered a lower bound.

Supplementary Figures and Tables

Table S1. Summary of compilation of dust deposition records.

Dust deposition site	Region	Type of record	Latitude	Longitude	Associated source(s)*	Record length	Approximate age resolution	Reference
NEGIS	Greenland	Ice core	75.62º	-35.96º	East Asia, North Africa, North America	1607 – 2005	1 year	Vallelonga et al. (2014)[31]
GISP2	Greenland	Ice core	72.6º	-38.5º	East Asia, North Africa, North America	665 – 1990	2-3 years (irregular)	Zielinski & Mershon (1997)[32]
20D	Greenland	Ice core	65.02º	-44.87º	East Asia, North Africa, North America	1767 – 1984	1 year	Kang et al. (2003)[33]
Mount Logan	Yukon, Canada	Ice core	60.58º	-140.5º	East Asia	1000 – 1998	1 year	Osterberg et al. (2008)[9]
Motianling	Great Hinggan Range, China	Peat core	47.35º	120.65º	East Asia	1860 – 2007	3-30 years (irregular)	Bao et al. (2012)[8]
Point d'Escuminac	New Brunswick, Canada	Peat core	46.92º	-65.5º	North America	1550 – 1996	4-25 years (irregular)	Kylander et al. (2009)[34]
San Juan Lakes	Colorado, USA	Lake sediment core	38º	-108º	North America	1855 - 2005	30 years	Neff et al. (2008)[18]
Dasuopo	Mount Xixiabangma, Himalaya	Ice core	28.38º	85.72º	Middle East / Central Asia	1450 – 1996	1 year	Thompson et al. (2000)[35]
Mount Everest #1	East Rongbuk Glacier, Himalaya	Ice core	28.03º	86.96º	Middle East / Central Asia	1690 - 2002	1 year	Kaspari et al. (2009)[36]
Mount Everest #2	East Rongbuk Glacier, Himalaya	Ice core	27.98º	86.92º	Middle East / Central Asia	1843 – 1997	1 year	Kang et al. (2003)[33]
Mauritania Canyon	Atlantic Ocean	Ocean sediment core	16.83º	-16.73º	North Africa	1180 BC – 2005	1-2 years	Mulitza et al. (2010)[6]
Sal Island	Cape Verde	Coral core	16.76º	-22.89º	North Africa	1955 – 2008	1 year	Evan & Mukhopadhyay (2010)[16]
Andros Island	Bahamas	Coral core	25º	-78º	North Africa	1065 – 2011	10-30 years (irregular)	Hayes et al. (2017)[4]
Colle Gnifetti	Italian Alpes	Ice core	45.94º	7.88º	North Africa	1780 – 2006	1 year	Clifford et al. (2019)[5]
Lake Bastani†	Corsica	Lake sediment core	42.07º	9.13º	North Africa	1220 BC - 2013	3-4 years	Sabatier et al. (2020)[7]; Pierre Sabatier, personal communication (2022)
Snowy Mountains	NSW, Australia	Peat core	-36.46º	148.3º	Australia	500 – 2005	2 – 10 years (irregular)	Marx et al. (2014)[37]
Law Dome	Budd Coast, East Antarctica	Ice core	-66.77º	112.8º	South America, Australia	1480 – 1996	1 year	Souney et al. (2002)[38]
Siple Station	Ellsworth land, West Antarctica	Ice core	-75.92º	-84.25º	South America, Australia	1417 – 1983	1 year	Mosley-Thompson et al. (1990)[39]
James Ross Island	Northern Antarctic Peninsula	Ice core	-64.2º	-57.7º	South America	1832 - 1991	1 year	McConnell et al. (2007)[17]

*Associated sources are based on Fig. S1.

[†]The data of Sabatier et al.[7] were further corrected for sediment matrix effects through centered-log-ratio (CLR) transformation (Sabatier, personal communication, 2022).

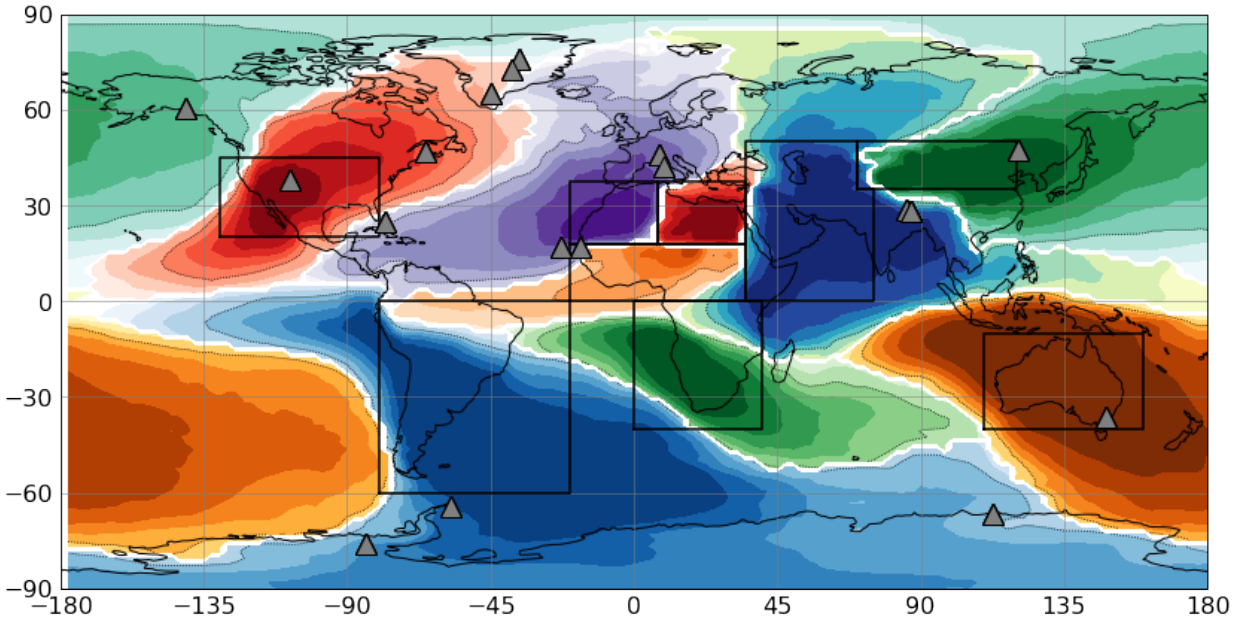

Figure S1. Map of deposition record sites and dominant dust source regions. Different colors represent the fraction of the dust deposition flux supplied by different dominant source regions, with shading decreasing in increments of 0.1 from a maximum of 1. The black boxes denote the nine major source regions (western North Africa, eastern North Africa, the Southern Sahara and Sahel, the Middle East & Central Asia, East Asia, North America, Australia, South America, Southern Africa). Gray triangles denote the locations of the 19 dust deposition records used to reconstruct dust loading since pre-industrial times. After Ref. [2].

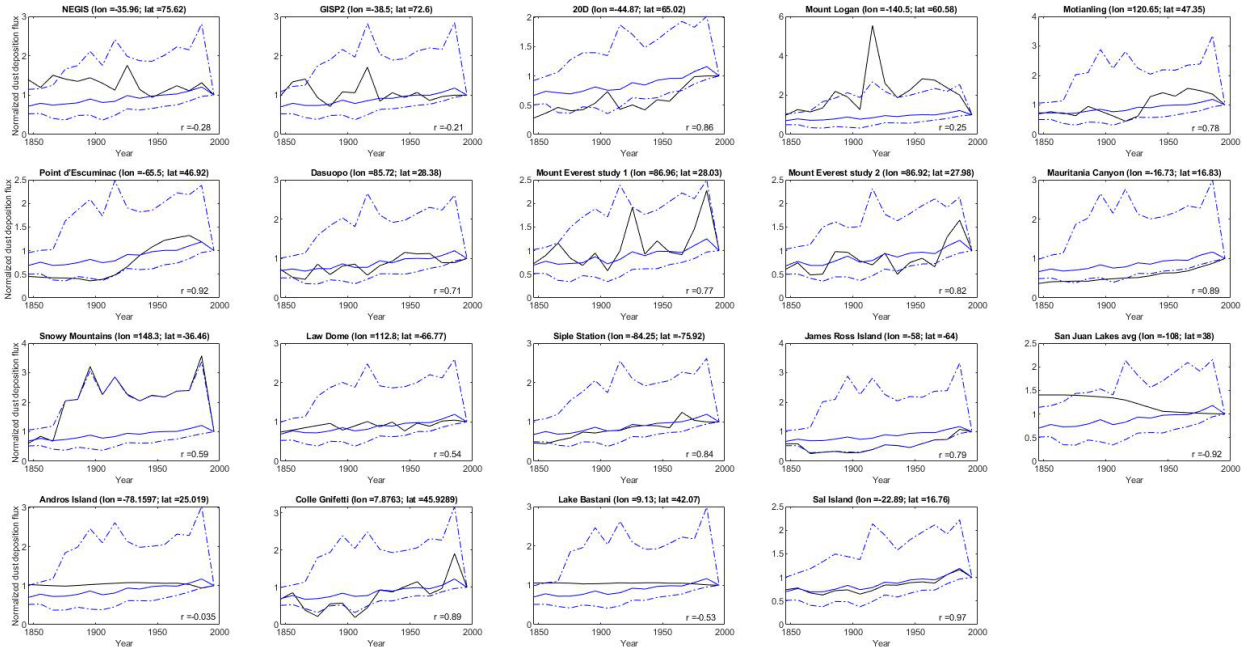

Figure S2. Comparisons between dust deposition records and reconstructed dust deposition fluxes. Shown are results for the 19 deposition records in our compilation (Table S1). The solid black line represents the measured normalized deposition fluxes (or deposition flux proxy) after data processing (see text), the solid blue line the median reconstructed normalized deposition flux, and the dash-dotted blue lines the one standard error interval on the reconstructed normalized deposition flux. Also listed is the correlation coefficient between the measured and median reconstructed normalized deposition fluxes.

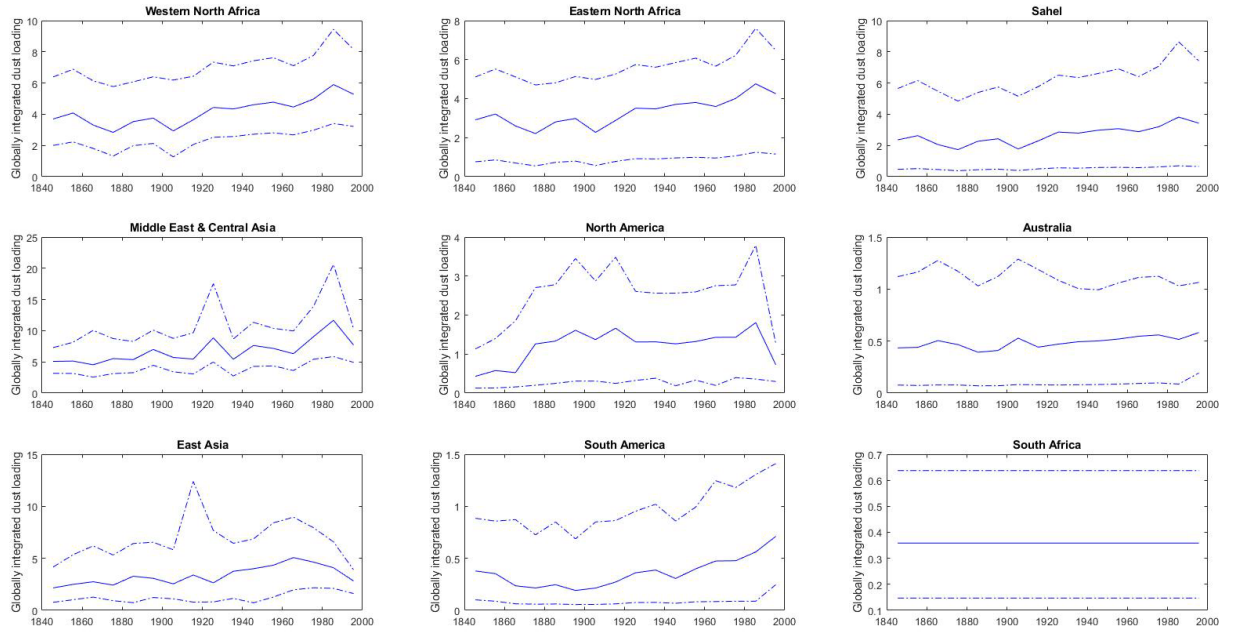

Figure S3. Reconstructed globally integrated dust loading for each source region. The solid line represents the median estimate and the dash-dotted lines the one standard error interval.

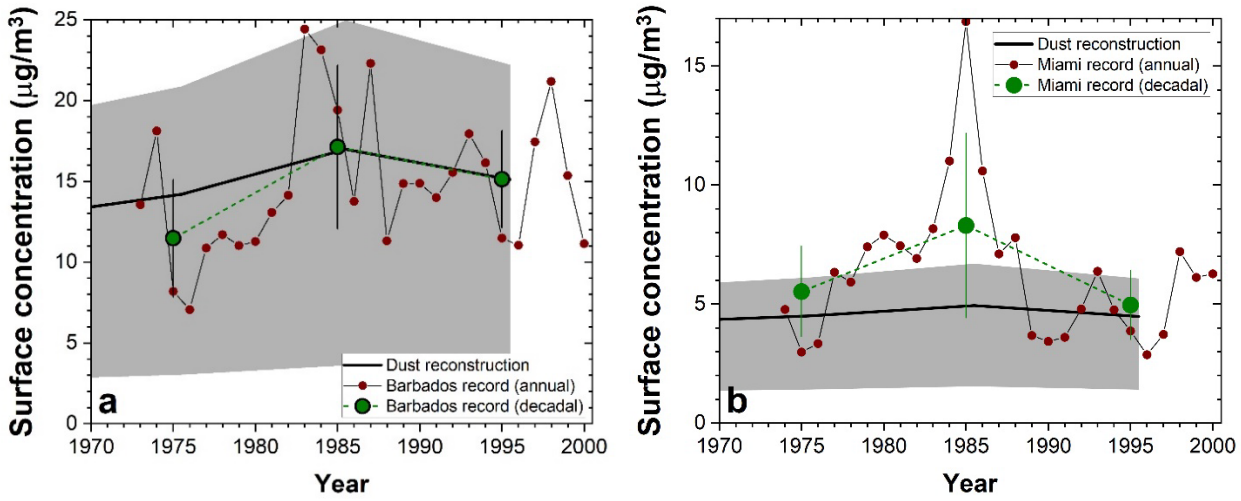

Figure S4. Comparison of dust reconstruction against long-term dust surface concentration measurements. a| Comparison against measurements at Barbados. **b**| Comparison against measurements at Miami. Small brown circles denote the measured annual average surface concentration, which was calculated from previously reported monthly average values[40]. Large green circle denote decadal averages of the annual values for a more direct comparison against the dust reconstruction. Error bars on the decadal values denote the standard deviation of the annual values. The solid black line denotes the median estimate of the reconstructed dust surface concentration and the shading denotes the 90% confidence range.

References

1 Kok, J. F. *et al.* Improved representation of the global dust cycle using observational constraints on dust properties and abundance. *Atmos. Chem. Phys.* **in press** (2021).

2 Kok, J. F. *et al.* Contribution of the world's main dust source regions to the global cycle of desert dust. *Atmos. Chem. Phys. Discuss. [preprint]* **in review** (2021). https://doi.org:10.5194/acp-2021-4

3 Mahowald, N. M. *et al.* Observed 20th century desert dust variability: impact on climate and biogeochemistry. *Atmos. Chem. Phys.* **10**, 10875-10893 (2010). https://doi.org:10.5194/acp-10-10875-2010

4 Hayes, C. T., McGee, D., Mukhopadhyay, S., Boyle, E. A. & Maloof, A. C. Helium and thorium isotope constraints on African dust transport to the Bahamas over recent millennia. *Earth and Planetary Science Letters* **457**, 385-394 (2017). https://doi.org:10.1016/j.epsl.2016.10.031

5 Clifford, H. M. *et al.* A 2000 Year Saharan Dust Event Proxy Record from an Ice Core in the European Alps. *Journal of Geophysical Research-Atmospheres* **124**, 12882-12900 (2019). https://doi.org:10.1029/2019jd030725

6 Mulitza, S. *et al.* Increase in African dust flux at the onset of commercial agriculture in the Sahel region. *Nature* **466**, 226-228 (2010). https://doi.org:10.1038/nature09213

7 Sabatier, P. *et al.* Past African dust inputs in the western Mediterranean area controlled by the complex interaction between the Intertropical Convergence Zone, the North Atlantic Oscillation, and total solar irradiance. *Clim. Past.* **16**, 283-298 (2020). https://doi.org:10.5194/cp-16-283-2020

8 Bao, K. S. *et al.* Recent atmospheric dust deposition in an ombrotrophic peat bog in Great Hinggan Mountain, Northeast China. *Science of the Total Environment* **431**, 33-45 (2012). https://doi.org:10.1016/j.scitotenv.2012.05.014

9 Osterberg, E. *et al.* Ice core record of rising lead pollution in the North Pacific atmosphere. *Geophysical Research Letters* **35** (2008). https://doi.org:10.1029/2007gl032680

10 Chernick, M. R. *Bootstrap methods : a guide for practitioners and researchers*. 400 (Wiley-Interscience, 2007).
11 Efron, B. *The jackknife, the bootstrap, and other resampling plans*. (Capital City Press, 1982).
12 Hooper, J. & Marx, S. A global doubling of dust emissions during the Anthropocene? *Glob. Planet. Change* **169**, 70-91 (2018). https://doi.org:10.1016/j.gloplacha.2018.07.003
13 Albani, S. *et al.* Twelve thousand years of dust: the Holocene global dust cycle constrained by natural archives. *Climate of the Past* **11**, 869-903 (2015). https://doi.org:10.5194/cp-11-869-2015
14 Koffman, B. G. *et al.* Centennial-scale variability of the Southern Hemisphere westerly wind belt in the eastern Pacific over the past two millennia. *Clim. Past.* **10**, 1125-1144 (2014). https://doi.org:10.5194/cp-10-1125-2014
15 Rhodes, R. H. *et al.* Little Ice Age climate and oceanic conditions of the Ross Sea, Antarctica from a coastal ice core record. *Clim. Past.* **8**, 1223-1238 (2012). https://doi.org:10.5194/cp-8-1223-2012
16 Evan, A. T. & Mukhopadhyay, S. African Dust over the Northern Tropical Atlantic: 1955-2008. *Journal of Applied Meteorology and Climatology* **49**, 2213-2229 (2010). https://doi.org:10.1175/2010jamc2485.1
17 McConnell, J. R., Aristarain, A. J., Banta, J. R., Edwards, P. R. & Simoes, J. C. 20th-Century doubling in dust archived in an Antarctic Peninsula ice core parallels climate change and desertification in South America. *Proc. Natl. Acad. Sci. U. S. A.* **104**, 5743-5748 (2007). https://doi.org:10.1073/pnas.0607657104
18 Neff, J. C. *et al.* Increasing eolian dust deposition in the western United States linked to human activity. *Nature Geoscience* **1**, 189-195 (2008). https://doi.org:10.1038/ngeo133
19 Smith, M. B. *et al.* Sensitivity of the interannual variability of mineral aerosol simulations to meteorological forcing dataset. *Atmospheric Chemistry and Physics* **17**, 3253-3278 (2017). https://doi.org:10.5194/acp-17-3253-2017
20 Albani, S. *et al.* Paleodust variability since the Last Glacial Maximum and implications for iron inputs to the ocean. *Geophysical Research Letters* **43**, 3944-3954 (2016). https://doi.org:10.1002/2016gl067911
21 Bullard, J. E. *et al.* High-latitude dust in the Earth system. *Reviews of Geophysics* **54**, 447-485 (2016). https://doi.org:10.1002/2016rg000518
22 Kok, J. F. *et al.* Contribution of the world's main dust source regions to the global cycle of desert dust. *Atmospheric Chemistry and Physics* **21**, 8169-8193 (2021). https://doi.org:10.5194/acp-21-8169-2021
23 Cakmur, R. V. *et al.* Constraining the magnitude of the global dust cycle by minimizing the difference between a model and observations. *Journal of Geophysical Research-Atmospheres* **111**, D06207 (2006). https://doi.org:10.1029/2005jd005791
24 Stanelle, T., Bey, I., Raddatz, T., Reick, C. & Tegen, I. Anthropogenically induced changes in twentieth century mineral dust burden and the associated impact on radiative forcing. *Journal of Geophysical Research-Atmospheres* **119**, 13526-13546 (2014). https://doi.org:10.1002/2014jd022062
25 Avila, A., QueraltMitjans, I. & Alarcon, M. Mineralogical composition of African dust delivered by red rains over northeastern Spain. *Journal of Geophysical Research-Atmospheres* **102**, 21977-21996 (1997). https://doi.org:10.1029/97jd00485
26 Wu, C. C., Lin, Z. & Liu, X. The global dust cycle and uncertainty in CMIP5 (Coupled Model Intercomparison Project phase 5) models. *Atmospheric Chemistry and Physics* **20**, 10401-10425 (2020). https://doi.org:10.5194/acp-20-10401-2020
27 Ginoux, P., Prospero, J. M., Gill, T. E., Hsu, N. C. & Zhao, M. Global-scale attribution of anthropogenic and natural dust sources and their emission rates based on MODIS Deep Blue aerosol products. *Reviews of Geophysics* **50**, Rg3005 (2012). https://doi.org:10.1029/2012rg000388

28 Yu, H. B. *et al.* Estimates of African Dust Deposition Along the Trans-Atlantic Transit Using the Decadelong Record of Aerosol Measurements from CALIOP, MODIS, MISR, and IASI. *Journal of Geophysical Research-Atmospheres* **124**, 7975-7996 (2019). https://doi.org:10.1029/2019jd030574

29 Mahowald, N., Albani, S., Engelstaedter, S., Winckler, G. & Goman, M. Model insight into glacial-interglacial paleodust records. *Quat. Sci. Rev.* **30**, 832-854 (2011). https://doi.org:10.1016/j.quascirev.2010.09.007

30 Carslaw, K. S. *et al.* Aerosols in the Pre-industrial Atmosphere. *Current Climate Change Reports* **3**, 1-15 (2017). https://doi.org:10.1007/s40641-017-0061-2

31 Vallelonga, P. *et al.* Initial results from geophysical surveys and shallow coring of the Northeast Greenland Ice Stream (NEGIS). *Cryosphere* **8**, 1275-1287 (2014). https://doi.org:10.5194/tc-8-1275-2014

32 Zielinski, G. A. & Mershon, G. R. Paleoenvironmental implications of the insoluble microparticle record in the GISP2 (Greenland) ice core during the rapidly changing climate of the Pleistocene-Holocene transition. *Geol. Soc. Am. Bull.* **109**, 547-559 (1997). https://doi.org:10.1130/0016-7606(1997)109<0547:piotim>2.3.co;2

33 Kang, S. C. *et al.* Dust records from three ice cores: relationships to spring atmospheric circulation over the Northern Hemisphere. *Atmos. Environ.* **37**, 4823-4835 (2003). https://doi.org:10.1016/j.atmosenv.2003.08.010

34 Kylander, M. E., Weiss, D. J. & Kober, B. Two high resolution terrestrial records of atmospheric Pb deposition from New Brunswick, Canada, and Loch Laxford, Scotland. *Science of the Total Environment* **407**, 1644-1657 (2009). https://doi.org:10.1016/j.scitotenv.2008.10.036

35 Thompson, L. G. *et al.* A high-resolution millennial record of the South Asian Monsoon from Himalayan ice cores. *Science* **289**, 1916-1919 (2000). https://doi.org:10.1126/science.289.5486.1916

36 Kaspari, S. *et al.* A High-Resolution Record of Atmospheric Dust Composition and Variability since AD 1650 from a Mount Everest Ice Core. *Journal of Climate* **22**, 3910-3925 (2009). https://doi.org:10.1175/2009jcli2518.1

37 Marx, S. K. *et al.* Unprecedented wind erosion and perturbation of surface geochemistry marks the Anthropocene in Australia. *Journal of Geophysical Research-Earth Surface* **119**, 45-61 (2014). https://doi.org:10.1002/2013jf002948

38 Souney, J. M. *et al.* A 700-year record of atmospheric circulation developed from the Law Dome ice core, East Antarctica. *Journal of Geophysical Research-Atmospheres* **107** (2002). https://doi.org:10.1029/2002jd002104

39 Mosley-Thompson, E., Thompson, L. G., Grootes, P. & Gundestrup, N. Little ice age (neoglacial) paleoenvironmental conditions at siple station, Antarctica. *J. Glaciol.* **14**, 199-204 (1990).

40 Zuidema, P. *et al.* Is Summer African Dust Arriving Earlier to Barbados? The Updated Long-Term In Situ Dust Mass Concentration Time Series from Ragged Point, Barbados, and Miami, Florida. *Bulletin of the American Meteorological Society* **100**, 1981-1986 (2019). https://doi.org:10.1175/bams-d-18-0083.1